Deep Learning for Sea Surface Temperature Reconstruction under Cloud Occlusion

Andrea Asperti^a, Ali Aydogdu^b, Emanuela Clementi^b, Angelo Greco^a, Lorenzo Mentaschi^c, Fabio Merizzi^a, Pietro Miraglio^b, Paolo Oddo^c, Nadia Pinardi^c, Alessandro Testa^a

^a University of Bologna, Department of Informatics - Science and Engineering
(DISI), Via Mura Anteo Zamboni 7, Bologna, 40126, , Italy

^b CMCC Foundation - Euro-Mediterranean Center on Climate Change Viale Carlo Berti
Pichat 6/2, Bologna, 40127, , Italy

^c University of Bologna, Department of Physics and Astronomy (DIFA), Viale Carlo
Berti Pichat 6/2, Bologna, 40127, , Italy

Abstract

Sea Surface Temperature (SST) is crucial for understanding Earth's oceans and climate, significantly influencing weather patterns, ocean currents, marine ecosystem health, and the global energy balance. Large-scale SST monitoring relies on satellite infrared radiation detection, but cloud cover presents a major challenge, creating extensive observational gaps and hampering our ability to fully capture large-scale ocean temperature patterns. Efforts to address these gaps in existing L4 datasets have been made, but they often exhibit notable local and seasonal biases, compromising data reliability and accuracy. To tackle this challenge, we employed deep neural networks to reconstruct cloud-covered portions of satellite imagery while preserving the integrity of observed values in cloud-free areas, using MODIS satellite derived observations of SST. Our best-performing architecture showed significant skill improvements over established methodologies, achieving substantial reductions in error metrics when benchmarked against widely used approaches and datasets. These results underscore the potential of advanced AI techniques to enhance the completeness of satellite observations in Earthscience remote sensing, providing more accurate and reliable datasets for environmental assessments, data-driven model training, climate research, and seamless integration into model data assimilation workflows.

Keywords: Sea Surface Temperature, operational oceanography, weather

modeling, occlusion, reanalysis, reconstruction, inlining, completion, deep learning

1. Introduction

Sea Surface Temperature (SST) is a major parameter for understanding and modeling the earth climate system. Air-sea heat fluxes, depending on the sea surface and air temperatures are a major driver of the Earth's atmosphere dynamics. They greatly influence all the scales of motion from weather predictions to long-term climate trends. Further, SST being also the signature of ocean horizontal and vertical processes is a key parameter in the study of the ocean dynamics per-se (uncoupled).

Since the 1980s, satellites have been increasingly used to measure SST. The satellite measurement is typically made by sensing the ocean radiation in two or more wavelengths within the infrared part of the electromagnetic spectrum or other parts of the spectrum which can then be empirically related to SST. One difficulty of this approach is that infrared satellites - differently from microwaves ones - cannot look through clouds; considering that, on average, about 75% of the ocean surface is covered by clouds [1], the gaps in collected data are significant, and reconstructing SST under cloud occlusion conditions is a challenging and lively research topic. Traditional statistical techniques, such as Optimal Interpolation (OI) [2], Empirical Orthogonal Function (EOF) [3], and other similar techniques [4, 5], fill missing values based on spatial/temporal correlations between observed SST points. Present day L4 SST product from CMES is actually produced by a spacetime OI scheme described in [6].

A problem of statistical approaches is that they often struggle to resolve fine-scale features, resulting in overly smooth reconstructions [7, 8, 9]. These techniques typically assume linearity, which limits their ability to capture the complex dynamics of SST fields. Consequently, there has been growing interest in recent years in applying deep learning techniques to address this challenge. Convolutional autoencoders, such as DINCAE, have been successfully used to reconstruct SST and chlorophyll concentrations [9, 10, 11], while vision transformers trained with a masked autoencoder approach (MAESSTRO) have also been explored [12]. A recent survey of statistical and AI-based reconstruction methods for oceanographic data is available in [5].

Image completion — or image inpainting — is a well-researched area in image processing [13, 14, 15, 16, 17, 18, 19], with various techniques successfully applied across different domains. In this article, we evaluate some of these techniques for reconstructing Sea Surface Temperature in clouds covered regions. The method is applied to L3 images at the resolution of 4 km for a single sensor SST; particular attention is given to the model configuration and the calibration of the parameters.

The analysis is mainly done on a region comprising Italy and his surrounding Seas, described in the red box of Figure 1. The area covers 256x256 observation points with latitude between 35.33° and 46.0°E and longitude between 7.92° and 18.58°N, for a total domain extension of 1020 x 1020 squared kilometers. In the future, we plan to extend the analysis to the full Mediterranean Sea of Figure 1.



Figure 1: The red square describes the region of our investigation, with latitude between 35.33° and 46.0°E and longitude between 7.92° and 18.58°N.

The reconstruction obtained by our model was validated against the current L4 reconstruction [6] and the recent DINCAE model [9, 10], testifying in both cases a notable performance improvement.

The article is structured in the following way. In Section 2 we describe the dataset used in the work, based on MODIS-AQUA data. This section also contains an investigation of data, comprising gradients (subsection 2.2) persistence (subsection 2.3) and climatology (subsection 2.4). Our Methodology is explained in Section 3: part of data are subject to an additional obfuscation, creating an artificial ground truth for testing purposes. In Section 4, we introduce the main classes of models investigated in this article, namely U-Net models (subsection 4.1) and Visual Transformers (subsection

4.2). In this section we also discuss generators (subsection 4.3), in charge of the dynamic obfuscation of training data, and training (subsection 4.4). Our results are illustrated in Section 5. The final sections are devoted to ablation (Section 6) and conclusions (Section 7).

2. Data Set

Our investigation of Sea Surface Temperature is based on the NightTime MODIS dataset available at https://podaac.jpl.nasa.gov/dataset/MODIS_AQUA_L3_SST_THERMAL_DAILY_4KM_NIGHTTIME_V2014.0. Data have been acquired by the Moderate-resolution Imaging Spectroradiometer (MODIS) [20] on board the NASA TERRA and AQUA satellite platforms, launched in 1999 and 2002 respectively. For our investigation, we used the daily products at 4 km spatial resolution relative to nighttime passes.

We mostly worked with MODIS-AQUA data, using MODIS-TERRA for validation purposes. These are composed of

- sst / sst4 the SST measurements. Missing data are represented by NaNs. All nighttime measurements from 7/4/2002 to 12/31/2023 were used. Part of the data, from 7/4/2021 to 12/31/2023, was used for testing purposes.
- qual_sst / qual_sst4 quality flags for the data. They go from 0 (best) to 5 (worst). Our data only has measurements of quality 0, 1 and 2, respectively amounting 68.29%/30.56%/1.14% of diurnal data and 79.10%/20.73%/0.17% of nocturnal data.

Each measurement also has associated metadata. Info can be found on the Ocean Data Product Users Guide.

The MODIS-TERRA dataset was previously used in [9, 10] for training and validation. We compare with these results in Section 5.2.2.

2.1. Data analysis

In this section, we investigate the datasets, pointing out a few critical aspects of collected data, typically due to problems of the signal in proximity of the coast, or at the border of clouds.

In Table 1 we show the minimum and maximum value of the temperature for the day and night datasets.

day			night		
min avg max		min avg max		max	
1.3	20.9	34.9	0.1	20.5	31.1

Table 1: Minimum and maximum values of SST for day and night from MODIS-AQUA. Note the low minimum values, unrealistic in the case of the seawaters in the Mediterranean Sea.

The seawater temperature at large scales never falls below $5^{\circ}C$, as shown in the histogram in Figure 2, with the lowest values of the distribution associated with shallow coastal waters. The minimum temperatures in Table 1 likely reflect cloud edges not accurately captured by the cloud detection algorithm. The number of these outliers is very small, and their impact is negligible.

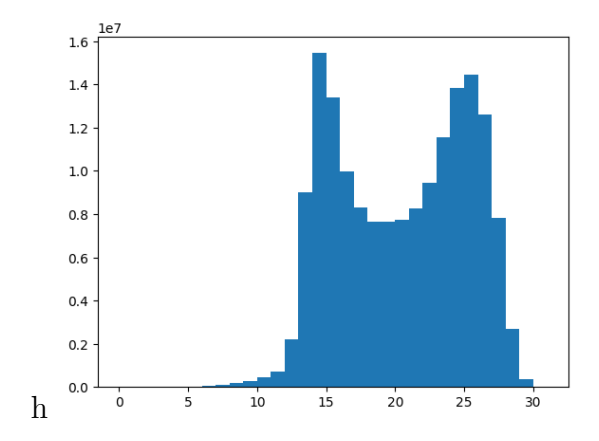


Figure 2: Histogram relative to the distribution of MODIS-AQUA nightly temperatures, cumulative over all spatial positions and all years.

2.2. Gradients

Gradients in sea surface temperatures (SSTs) play a crucial role in shaping atmospheric circulation, influencing weather systems, and regulating heat exchange between the sea and atmosphere. Here, we define gradients as variations in adjacent positions within our SST data grid, measured along both spatial and temporal axes. Table 2 presents statistics related to these gradients.

Spatial gradients are generally low, with an average fluctuation around 0.15° for a resolution of 4 km. However, these fluctuations are not uniformly

	temporal axis				spatial axis			
	max	avg max	mean	std	max	avg max	mean	std
day	9.31	4.08	0.73	0.71	10.47	2.95	0.14	0.16
night	8.20	3.96	0.37	0.38	8.10	3.45	0.15	0.20

Table 2: Statistics on the spatial and temporal temperature gradients, measured as differences between neighboring grid points (spatial axis) or consecutive days (temporal axis).

distributed: larger gradients are typically observed near coastal areas (see Figure 3(a)), particularly along the western coast of the Adriatic Sea and the Sicilian coast of the Strait of Sicily.

There are also sporadic cases where significantly higher gradients are observed. In some days, larger gradients are found in the open ocean around large scale oceanic features. An example is given in Fig.3(b), where the maximum gradients are around the southern border of the Northern Tyrrhenian Gyre [21], near the Strait of Bonifacio. In the majority of the cases, the extreme gradient values are along the coasts as expected and around the cloud borders (Fig.3(c)), due to satellite detection accuracy.

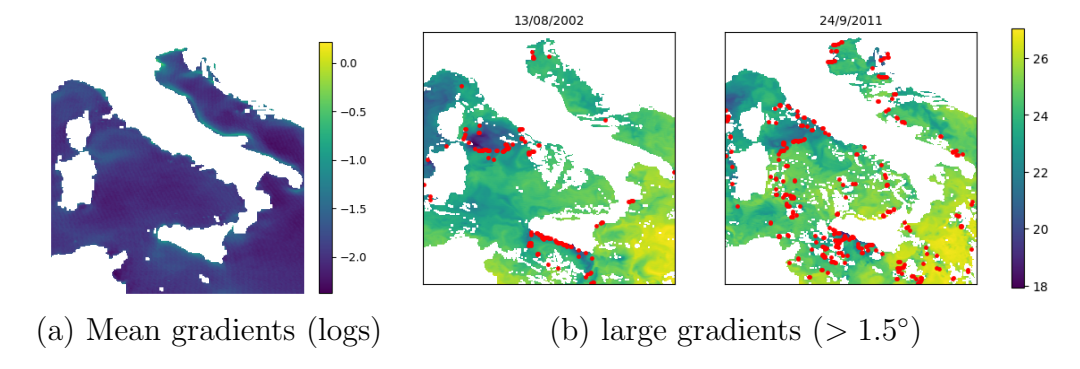


Figure 3: Spatial Gradients. On the left (a) the average spatial gradients expressed in logarithm. On the right (b) example of large spatial gradients for two specific days.

In any case, high spatial gradients are quite rare. Table 3 shows the percentage of points with extreme gradients, considering thresholds between 1 and 3 degrees.

On the other hand, significant daily fluctuations at the same location are relatively common. The mean temporal variation from one day to the next is around 0.37° for nighttime observations, and nearly double for daytime measurements (see Table 2). Additionally, the tail of extremely high daily

	> 1°	$> 1.5^{\circ}$	> 2°	$> 2.5^{\circ}$	> 3°
night:time	1.05%	0.96%	0.87 %	0.80%	0.74%
night:spatial	0.29%	0.094%	0.037%	0.017%	0.008%

Table 3: Frequency of high spatial and temporal gradients in MODIS-AQUA data relative to the region of interest. In the spatial case, the "gradient" refers to the difference in SST between two neighboring grid points, 4 km apart; similarly, for the temporal case, it is the difference in SST between two consecutive days at a given spatial position.

temperature variations appears to be particularly thick (see Table 3).

2.3. Persistence

Due to the large occlusions caused by clouds, it is natural to attempt using a temporal sequence of a few consecutive days to improve the accuracy of the reconstruction. This approach can be seen as a form of persistence, where we use the closest available data to fill gaps.

Unfortunately, the approximation provided by data from previous days is not very precise. Table 4 shows the difference for nighttime data, expressed in terms of both Mean Absolute Difference (MAD) and Root Mean Square Difference (RMSD), for increasing temporal gaps, ranging from 1 to 5 days. The diffeence is measured as an average over sea locations that are visible on both days.

The difference increases very rapidly, and the contribution to reconstruction from previous days is not immediately clear.

	1d	2d	3d	4d	5d
MAD	0.37°	0.50°	0.61°	0.70°	0.78°
RMSD	0.53°	0.69°	0.83°	0.95°	1.05°

Table 4: Average distance, in terms of Mean Absolute Difference (MAD) and Rooted Mean Squared Difference (RMSD) between the SST of a given day and those of previous days.

According to our experiments, reported in Section 5, considering temporal sequences longer than 4 consecutive days bring no improvement to the reconstruction.

2.4. Climatology

In the context of statistical averages, climatology refers to the long-term average of ocean state variables (temperature, currents, salinity, etc.) for a

specific region over a long time period. This average serves as a baseline or reference point to understand typical conditions in a given location and time of year. Climatology helps in identifying deviations from the norm (anomalies) and can be used to assess trends or patterns in climate behavior.

As it is clear from Fig.2, climatology has a strong seasonal cycle. In statistical analysis, tt is important to subtract the quasiperiodic signals in the time series such as the seasonal cycle. Thus we define a climatology as the daily time mean SST across all the 21 years of the dataset. Anomalies are then calculated by subcracting from each day the seasonal climatology.

The resulting daily climatology still suffer from small time gaps where data are absent for a particular day of the year, due to the presence of clouds.

To fill these gaps, we use interpolation, a mathematical technique that estimates unknown values based on surrounding data. In this case, a Gaussian blur is applied, which uses nearby spatial values to estimate missing ones. The Gaussian function gives more weight to closer values, while gradually reducing the influence of distant points.

The application of a Gaussian blur to a matrix with NaNs is not entirely straightforward. Simply replacing NaNs with zeros would treat them as valid values, flattening the result. Therefore, we need to reweight the result according to the average of the filter weights corresponding to meaningful (non-NaN) locations.

The interpolation process is divided into the following stages:

- 1. Replacement of missing values. The missing values (NaN) are replaced with zeros in the data matrix.
- 2. Application of the Gaussian filter. A Gaussian filter is applied to the resulting matrix, creating a "blurred" (biased) version of the data.
- 3. Generation of a binary mask. A second matrix is created to track the originally known points, assigning a weight of 0 to points with missing values and 1 to known points.
- 4. Application of the Gaussian filter to the mask. The resulting weights matrix describes the actual contribution of the region under the filter.
- 5. Division of matrices. The blurred data matrix is divided by the weights matrix to correct the original bias.

In the final division, the denominator may be 0, corresponding to a region in the input entirely composed of NaNs. In this case, mathematical libraries

usually produce a NaN. After applying the filter, a few NaNs may still remain, which can be filled by iterating the technique or using other interpolation methods.

The previous algorithm can be briefly described by the following code, in numpy style.

Algorithm 1 Gaussian Blur Interpolation with NaNs

- 1: **Input:** Data matrix D with NaNs, Gaussian filter G
- 2: Output: Interpolated matrix $D_{interpolated}$
- 3: $D_{copy} = D.copy()$
- 4: $D_{zeroed} = D_{copy}[np.isnan(D)] = 0$
- 5: $D_{blurred} = gaussian_filter(D_{zeroed}, G)$
- 6: M = np.where(np.isnan(D), 0, 1)
- 7: $W = gaussian_filter(M, G)$
- 8: $D_{interpolated} = D_{blurred}/W$

 \triangleright make a copy of D

⊳ replace NaN with zero

 \triangleright apply G to D_{zeroed}

⊳ create a bynary mask

 \triangleright apply G to the mask M

▷ correct the bias

It is worth mentioning that we interpolate both spatially and temporally to take advantage of persistence and produce a smoother climatology along the temporal axis.

We also considered an "unbiased" version of the climatology, where we adjust the mean SST of the baseline towards the observable temperature of the day under consideration.

Figure 4 shows an example of the climatology and its unbiased version.

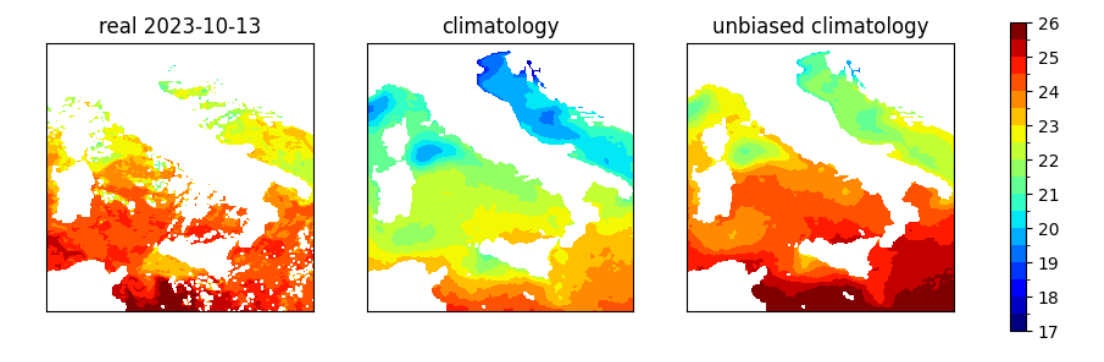


Figure 4: On the left, the nighttime SST data from a sample day, in this case 13/10/2024; in the middle the climatology of that day of the year; on the right the climatology adjusted (shifted) to the mean of the specific day.

As is evident from the figure, both the baseline and its unbiased version have limitations. The statistical baseline can differ significantly from the specific day under consideration, while the unbiased version is usually closer to reality but may negatively impact specific regions of the grid.

3. Evaluation Methodology

The training/evaluation of the reconstruction model is not straightforward since we do not have a ground truth for comparison. A traditional approach, as followed in [9, 10], involves creating an artificial ground truth by extending the occluded area in the source image and restricting the evaluation to this region.

This approach is schematically described in Figure 5. We start with a real image and compute the occlusion mask, corresponding to NaN values in the input (real mask). We then extend the masked area by superimposing the mask of a different day (artificial mask). The difference between the artificial mask and the real mask will define the region of the input where the reconstruction will be assessed (diff mask).

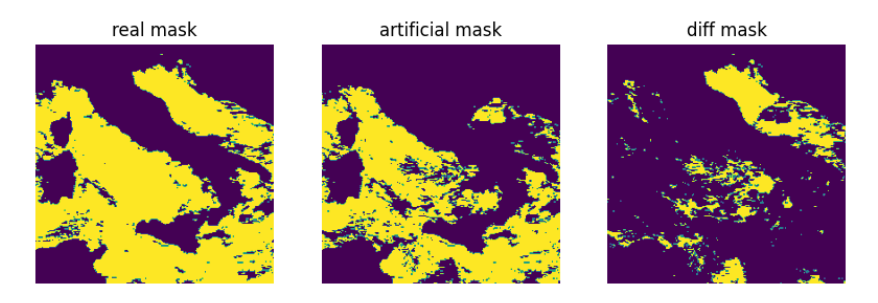


Figure 5: The first mask (real) describes the visible portion of the see. The second one (artificial) is the additional occlusion used for training. The final mask (diff) describes the points used as "ground truth", corresponding to locations visible in the current image, but artificially occluded.

This approach risks introducing biases since the sea temperature under clouds is usually different from the temperature under a clear sky. This bias is lower during the night, so the evaluation is typically restricted to night data.

In our approach, data are produced by a random generator that composes masks. The amount of occlusion in the source image, the maximum amount of additional occlusion, and the minimum size of the area in the diff mask available for evaluation are parameters that can be configured by the user and possibly dynamically changed during training. More details on the generator are given in Section 4.3.

An example of reconstruction is given in Figure 6. The first image is the actual input of the model, obtained by an artificial occlusion of the second (real) image; the third image is the reconstruction returned by the model, while the last one is a statistical baseline used for comparative purposes.

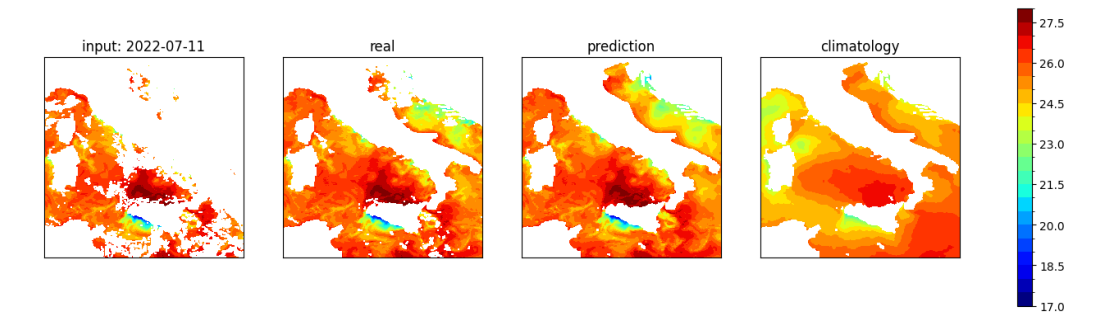


Figure 6: The image on the left is the input of the model; this is created by the generator through an artificial occlusion of the second (real) image; the third image is the reconstruction returned by the model; the image on the right is the climatology, used for comparative purposes.

It is interesting to observe that, in spite of the heavy occlusion of the input, the model is able to correctly reconstruct many details of the real image. Qualitative and quantitative evaluations will be given in Section 5.

4. Models

We tested several different neural network architectures, including variants of U-Net [22], Visual Transformers [23], and Diffusion Models [24, 25]. Each model was evaluated across a wide range of configurations, varying input dimensions, the number of channels, network depth, and incorporating specific modules such as attention layers or inception modules. So far, we have not achieved satisfactory results with diffusion models, so we will not report on those results.

Special attention was given to determining the optimal size of the geographical area under investigation. Experimentally, we found that splitting the original 256x256 region into four smaller areas, each 128x128 in size, and training four separate models resulted in better performance. Another key focus of the experimentation was determining the appropriate length of the temporal sequence of consecutive days to be used as input to the model.

In this section, we briefly introduce the two main classes of models: U-Net and Visual Transformers (ViT), as well as the training methodology. Experimental results will be presented in Section 5.

4.1. U-Net

The U-Net is a type of convolutional neural network (CNN) originally designed for biomedical image segmentation. Its architecture is structured as a U-shaped network, consisting of two main parts: the contracting path (encoder) and the expansive path (decoder). The encoder progressively reduces the spatial dimensions of the input image through convolutional and pooling layers, capturing increasingly abstract and high-level features. The decoder, on the other hand, upsamples these feature maps back to the original input size, enabling precise localization of the output reconstructions. The number of downsampling layers and their respective number of channels are key hyperparameters of the network. For example, a U-Net with the structure [64, 128, 256, 512] refers to a model with three downsampling layers that progressively halve the spatial dimensions while increasing the depth from the initial 64 channels to 128, 256, and 512 channels, respectively.

A key innovation of U-Net is the use of skip connections between corresponding layers in the encoder and decoder. These connections transfer high-resolution feature maps from the encoder to the decoder, allowing the model to combine both coarse and fine-grained information during reconstruction. This design makes U-Net highly effective for tasks where detailed output is essential. The U-Net was also already used in the Task of cloud occlusion: the model used in [9, 10] is essentially based on two U-Net composed in cascade.

The detailed architecture of our models is described in Figure 7. Don-wnsampling and upsampling blocks are composed by a short a short, configurable sequence of Residual Blocks, as described in Figure 8.

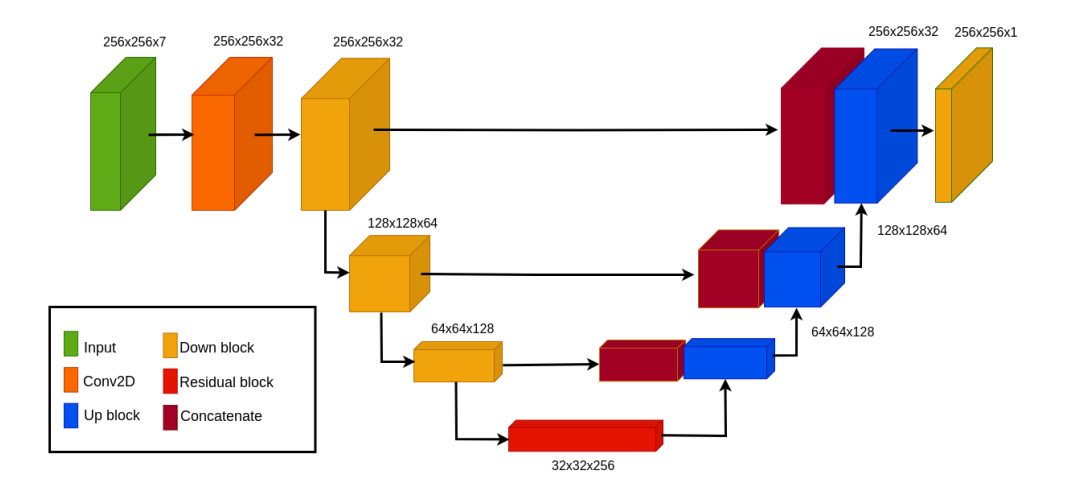


Figure 7: Basic Unet. In our terminology, this Unet has a [32,64,128,256] structure, meaning that is is composed of three downsampling blocks progressively halving the spatial dimension, and increasing the channel dimension to 64, 128 and 256. The initial spatial dimension is 256x256. The initial number of channels is 7, corresponding to three input days with the associated masks and the land-sea mask.

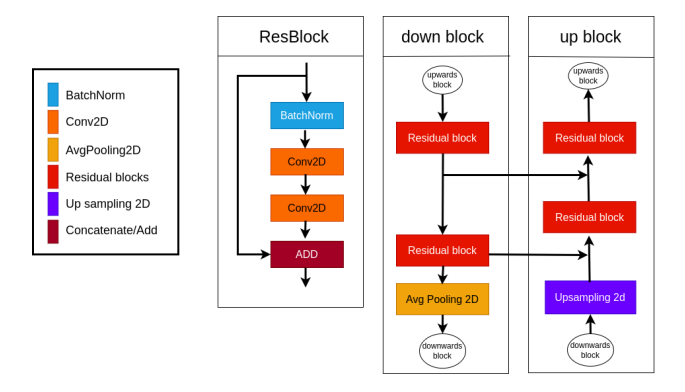


Figure 8: Upsampling and Downsampling blocks consist of Residual Blocks, exploiting resdual connections.

4.2. Visual Transformer

The Visual Transformer (ViT) [23] is a deep learning architecture designed for image recognition tasks, leveraging the transformer model [26], which was originally developed for natural language processing. Unlike traditional convolutional neural networks (CNNs) that rely on convolutions to capture spatial information, ViTs use self-attention mechanisms [27] to model

the relationships between different parts of an image.

In the ViT architecture (see Figure 9), an image is divided into fixed-size patches, which are then flattened and projected into embeddings, similar to how words are handled in transformers for language tasks. These patch embeddings are then processed by the transformer layers, which apply multihead self-attention to capture global dependencies across the entire image. This approach allows ViTs to capture long-range dependencies and context more efficiently than CNNs, especially for large-scale image datasets. ViTs have demonstrated state-of-the-art performance in various vision tasks and are particularly effective when trained on large datasets.

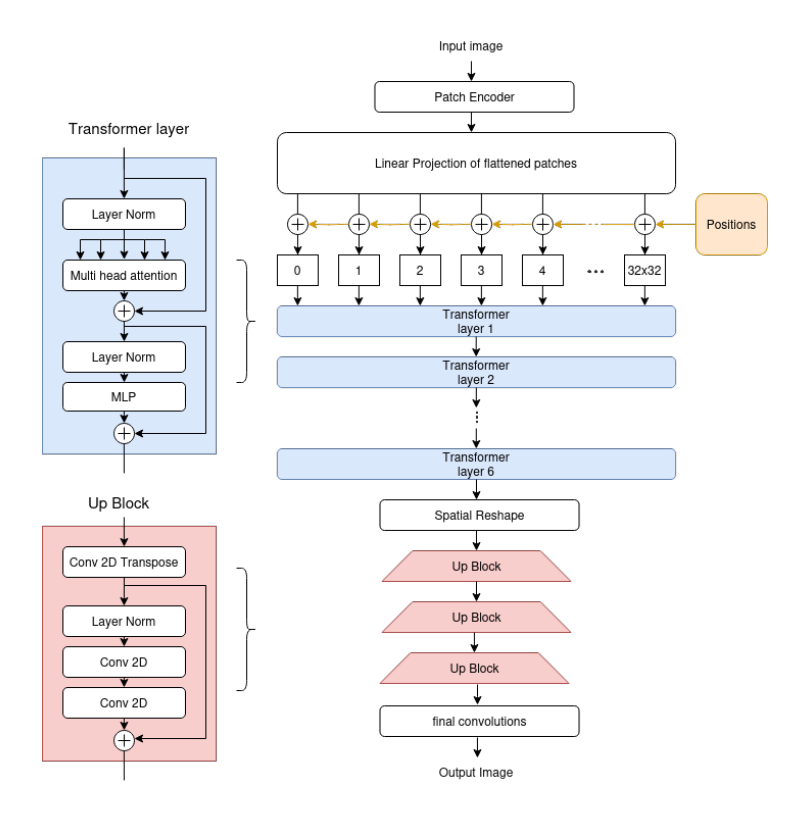


Figure 9: ViT Model. The source image is divided into fixed-size patches that, after embedding, are then processed by the transformer layers. Transformer layers use multihead self-attention to capture global dependencies across the entire image. Observe the final upsumapling blocks, peculiar to our implementation.

Relatively to the topic of cloud occlusion, a ViT model was used in [12], where a random subset of SST patches is masked or removed at training

time, mimicking a larger cloud occlusion. Afterward, a set of learnable mask tokens is added to the encoded patches before they are passed to the decoder, that reconstructs the original SST tile in pixel format.

In the usual ViT structure, after reassembling patches in their original spatial arrangement there is no further processing, and the output is directly produced in pixel format. However, we experimentally found convenient to add a few convolutional layers, also to recover the original spatial dimension of the input through a suitable number of upsampling operations, instead of a mere reshaping.

4.3. Generator

The generator implements the methodology explained in Section 3, which involves creating an artificial area that is known for validation but not visible during training. This area is generated by superimposing clouds from a different, randomly chosen day onto the current day. The process is done on the fly, and its stochastic nature ensures an almost infinite supply of varied training data.

The generator begins by selecting a random day from the nighttime dataset, ensuring that the chosen image has at least 40% of visible sea, to avoid working with insufficiently informative images. For each selected day, SST measurements relative to a given, configurable number of previous days are also retrieved. This approach enables the network to capture both spatial and temporal information, allowing the model to use historical data to reconstruct missing areas in the current image.

An artificial mask is created by extending the cloud cover from the current day with data from a random day. The clouds are selected in such a way to guarantee a minimum percentage of visible sea (typically, 5%), while ensuring at the same time that the new occluded area covers at least 10% of the sea area. Again, this two ranges are easily configurable. The overall procedure is meant to ensure that the image has enough occluded areas to support meaningful training and validation. Artificial masks are also applied to the previous days, preserving temporal continuity.

The generator's output is divided into two parts:

• Input data (batch_x): A 3D matrix with $2 \times s + 1$ channels, including the ortifically occluded images and masks for s days, and a land-sea mask.

• Target data (batch_y): A 3D matrix with 3 channels containing the actual SST image of the current day, the real mask identifying the clouds, and a "diff_mask" that highlights areas with artificial masking, used for monitoring and validation purposes.

For temperature reconstructions, the baseline temperature must be re-added to the denormalized data, after processing. The correct baseline can be either added as and additional output to batch_y or retrieved based on the date indices for each batch.

4.3.1. Testing configuration

The average percentage of visible sea in nightly MODIS data relative to the Italy region is around 46%. With the configuration of the generator described before, we obtain an average visibility around 25%, with an average additional cloud occlusion (the dimension of diff_mask) above 40%. This is good for training, since we expose the model to relatively challenging situations, but it is a bit unrealistic during testing. This is a delicate point since, not surprisingly, the performance of the model depends from the degree of occlusion of the input image, that becomes a crucial parameter of the evaluation. All results given in Section 5 are relative to a generator with a percentage of visible sea similar to those of real data.

4.4. Training

The training was performed on the Leonardo supercomputer at Cineca's high-performance computing center. Four nodes were used, each equipped with:

- 1 CPU Intel Xeon 8358 32 cores, 2,6 GHz
- 512 (8 x 54) GB RAM DDR4 3200 MHz
- 2 Nvidia HDR card 100 Gb/s per card
- 4 Nvidia custom Ampere GPU 64GB HBM2

Networks have been developed in the Tensorflow/Keras framework, and trained using the recent AdamW optimizer, which adapts the learning rate during training, combining it with weight decay. The starting learning rate was 1e-4.

Training was conducted with a maximum limit of 200 epochs with early stopping, using a batchsize of 32. For most configurations, training stops in less than 100 epochs, due to the early stopping callback. Training exploits a training generator, creating on the fly the augmentation in cloud occlusion described in Section 4.3.

At the end of each epoch, a validation phase is executed monitoring the loss on a suitable validation generator.

Various callbacks were used during training to improve model stability and performance and to perform real-time evaluations:

- Early Stopping: Training is stopped early if the validation loss does not improve for a given number of consecutive epochs, called patience. In our case, patience was set to 10.
- ReduceLROnPlateau: If the validation loss does not improve for 10 epochs, the learning rate is halved, until reaching a minimum value of 1e-5. This allows for smaller, more precise updates to the model in later training stages, ensuring higher performance.
- ModelCheckpoint: Whenever the validation loss improves, the model weights are saved to enable restoring the best model for further training.
- **TestCallbackGaussian**: A custom callback evaluates the model using RMSE at set intervals, for monitoring purposes.
- **TestCallbackGaussianDincae**: Similar to the previous callback, but the model is evaluated using DINCAE data, discussed further in Chapter **5.2.2**.

5. Experimental results

In this section we report the experimental results of the model. We divide it into two subsections. In the fist part we compare the performance of different models, and different configurations. The purpose of this analysis is to identify the best model for this task, as well as relevant information relative to the input, especially concerning the most suitable spatial and temporal dimensions of data. In the second section, we validate the performance of the model in two different ways, the first one using the current L4 reconstruction of CMES, and the second one by a comparison with the state of the art DINCAE model [9, 10].

5.1. Model comparison

In this section, we summarize the results of our experiments on the most significant networks investigated. We primarily compare three models: two U-Nets and a ViT. The two U-Nets, referred to as U-Net32 and U-Net64, differ in the number of channels, with the latter having double the number of channels. Both models have three downsampling layers, with a topology of [32,64,128,256] for U-Net32 and [64,128,256,512] for U-Net64. The numbers 32 and 64 in the network names correspond to the initial number of channels, before downsampling. The number of parameters for the three models is provided in Table 5.

	U-Net32	U-Net64	ViT
params	4,259,489	17,022,273	5,918,081

Table 5: Number of parameters for the models. The numbers refer to the versions with 11 input channels (5 days). Shorter sequences do not notably change the total number of parameters.

For each model, we consider two variants with different spatial dimensions: 128x128 and 256x256. The 128x128 model is actually a combination of four models, each trained on a different region of the input image. In this case, the evaluation metric is the average performance across the four models.

Additionally, we vary the number of consecutive input days used for reconstructing the SST, from day t (current day) to day t-s. We do not consider future days in the reconstruction.

The performance matric used is the Root Mean Square Error (RMSE) calculating the difference from the reconstructed SST under an artificial mask point and the real SST at that point. The average is measured using the test generator across a total of 50 batches, each consisting of 32 samples (for a total of 1,600 days). The RMSE measured in this manner is quite stable, with a standard deviation below 0.002 degrees.

As explained in Section 4.3.1, for evaluation purposes we used a generator providing an average percentage of visible sea around around 46%, that is similar to real data. More stressful situations are briefly investigated at the end of this section.

Results reported in Table 6 are truncated to the last significant digit.

Increasing the number of consecutive input days leads to a modest improvement in performance, though this effect stabilizes after 4 days. This is

days	U-Net32		U-Net64		m ViT	
	256×256	$128 \times 128 (\times 4)$	256×256	$128 \times 128 (\times 4)$	256×256	$128 \times 128 (\times 4)$
1	0.36	0.33	0.35	0.32	0.38	0.36
2	0.35	0.32	0.34	0.31	0.36	0.34
3	0.35	0.31	0.34	0.30	0.35	0.33
4	0.34	0.31	0.33	0.30	0.35	0.33
5	0.34	0.31	0.33	0.30	0.35	0.33
6	0.34	0.32	0.33	0.30	0.35	0.33

Table 6: Performance of the different models, measured in RMSE. The different rows refer to the number of consecutive days passed as input to the model. Values refer to data with an average percentage of visible sea around 46%. Splitting the model in 4 models with lower spatial dimension consistently gives better results.

consistent with our investigation of the persistence, in Section 2.3. On the other side, splitting the model into smaller geographical regions of dimension 128x128 each, results in a significant boost in performance.

In Table 7 we report the detail of the RMSE for the four quadrants over Italy; the values refer to our best model, namely U-Net64 with 4 days in input.

quadrant	NW	NE	\mathbf{SW}	\mathbf{SE}	Mean
RMSE	0.305	0.283	0.304	0.314	0.302

Table 7: RMSE reparted by quadrant. The values refer to U-Net64, with 4 days in input. Apparently, the Adriatic is the region with the best reconstruction accuracy, while the most complex one is the Ionian sea.

Many more models and variants of the previous one have been investigated. They are briefly discussed in Section 6.

To conclude this section, we present a brief investigation into the model's behavior under stress conditions. A positive feature of our configurable generator is its ability to easily adjust the maximum percentage of visible sea in the model's input. Figure 10 illustrates the relationship between visible sea percentage and RMSE, with each point representing a batch of 32 days. The plot corresponds to a U-Net32 model with 3 input days, though similar behavior is observed across other models.

As expected, performance degrades with higher levels of occlusion, but this degradation is nearly linear and not particularly severe. According to

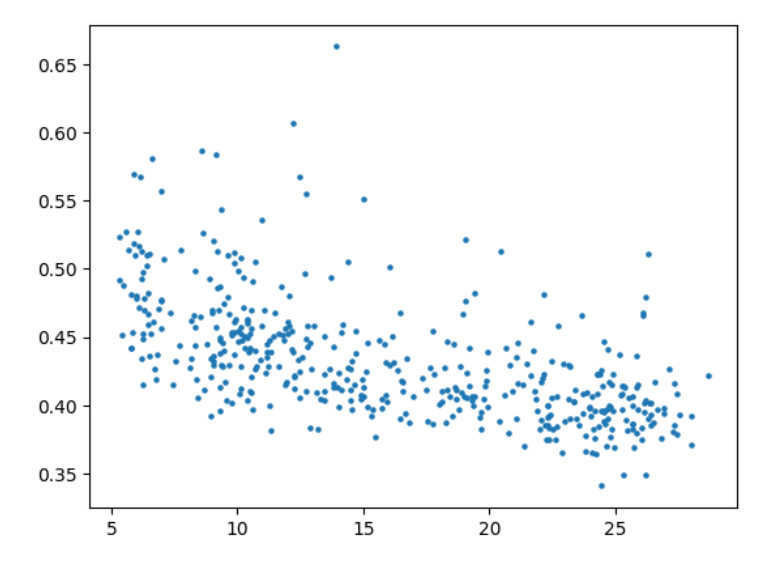


Figure 10: Degradation of the reconstruction error (vertical axis) in relation to the percentage of visible sea (horizontal axis). Each point is a batch of 32 days.

our investigations, there is an incremental error of approximately 0.005° for each additional percentage point of sea occlusion.

5.2. Validation

Validation was conducted in two ways: by comparing the results with the current statistical L4 reconstruction available from MODIS, and by comparing them with DINCAE, a similar data-driven approach to ours.

5.2.1. L4 comparison

L4 data in the context of MODIS (Moderate Resolution Imaging Spectro-radiometer) refers to a gridded dataset that provides gap-filled, interpolated, and temporally averaged sea surface temperature (SST) measurements. Unlike raw satellite observations, which may contain missing data due to cloud cover or other obstructions, L4 products use advanced algorithms to reconstruct continuous SST fields by filling in these gaps. This is typically done using statistical methods or model-based approaches that leverage spatial and temporal correlations.

L4 SST products are often derived from multiple satellite observations (such as from MODIS or other sensors) and provide high-resolution, daily or longer-term average temperature estimates. These data are essential for

various applications, including climate monitoring, oceanography, and environmental studies, as they offer a consistent and complete picture of sea surface temperatures over time.

The current technique used to reconstruct interpolated L4 data is based on an algorithm discussed in [6]. The model take advantage of most of the available sensor data in the infrared domain, comprising MODIS-TERRA and MODIS-AQUA. Since MODIS-AQUA is an input to the model, we would have expected to have an almost precise L4 reconstruction of SST in regions where the signal is available. Somewhat surprisingly, this is not the case.

The RMSE is quite high, around 0.49 degrees. In Figure 11, we compare the distribution of the error over the 12 months of year for L4 and our own reconstruction, specifically for a U-Net32 with 3 input days. In the case of L4 the error is mostly localized in the central months of the year: May, June and July. The error of our models is more uniform, and particularly low in the period from January to March. In our case, the error is measured using the generator, since the error in visible portions of the image is negligible.

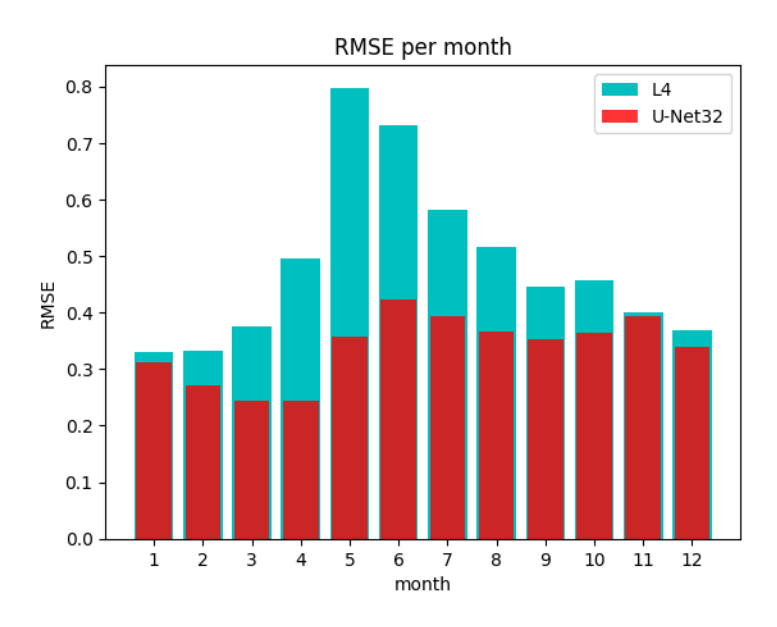


Figure 11: Distribution of the RMSE error over the 12 months of the year for L4 and our reconstruction model.

In Figure 12 we qualitatively compare our reconstructions with those offered by L4 reanalysis. Our reconstruction is more faithful to the ground truth and produces a more detailed output.

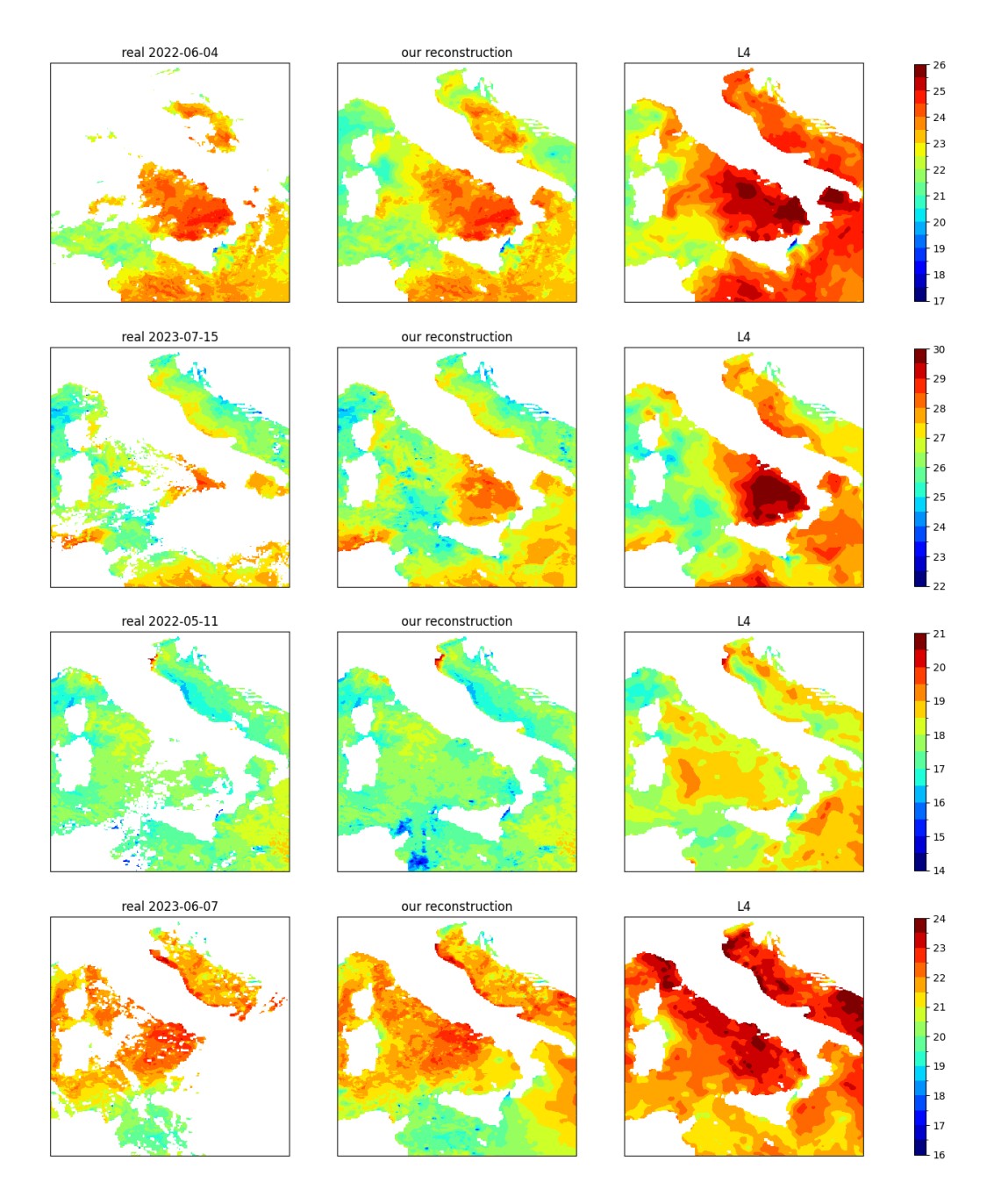


Figure 12: Visual Comparison between our reconstruction and L4.

5.2.2. Dincae

In this section, we compare the performance of our model with that of another state-of-the-art data-driven model: the Data INterpolating Convolutional Auto-Encoder (DINCAE) [9, 10].

The comparison was made using data directly provided by the authors of DINCAE. The comparison data are daily and at the same resolution as the data on which our model was trained, originating from nighttime SST measurements by the MODIS-TERRA satellite from 1/1/2003 to 12/31/2016. These data are divided into two datasets: one with artificially added coverage and the other with original data. Unlike our approach, the additional coverage is fixed and not configurable.

Since the DINCAE2 test focuses on the Northern Adriatic Sea, the analysis area differs from the one used by our model but largely overlaps. This area extends in latitude from 40° to 46° and in longitude from 12° to 19°. Therefore, to fit within the coordinates of our analysis area (latitude between 35.33° and 46.0°, and longitude between 7.92° and 18.58°), a vertical strip 10 pixels wide on the right side of the original 144x168 grid was trimmed, resulting in an overlapping area of 144x158.

To perform the comparison on these data without needing to change the dimensions or coordinates of the inputs of our models, the DINCAE datasets are cropped and positioned in a 256x256 matrix at their corresponding coordinates, with the rest of the matrix considered as obscured (see Figure 13). During evaluation, only the relevant portion of the data is taken into account.

In the case of models with a spatial dimension of 128x128, for simplicity, only the model from the North-East quadrant is used. To obtain an image of the correct size, an additional 10 pixels are cropped from the bottom and 30 from the left (in addition to the 10 pixels already removed from the right).

From the model's perspective, DINCAE [9] is essentially a double U-Net, where two networks are composed in cascade. Unlike our model, which only uses the available SST information, DINCAE incorporates additional indicators, including the date and wind speed, which are further extended in DINCAE2 [10] to account for the amount of chlorophyll.

In Table 8, we compare the RMSE of DINCAE (best model, with clorophyll) and our 4-days models, outperforming it by a sensible margin.

In this case too the best model is the U-Net64 with spatial dimension 128x128, although all models show interesting performances.

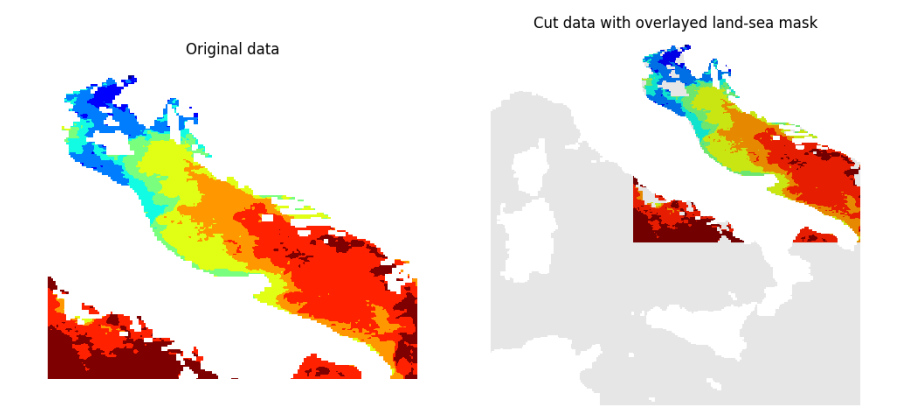


Figure 13: On the left is the DINCAE SST measurement from April 15, 2003. On the right, this measurement is cropped and repositioned in a 256x256 matrix, maintaining the coordinates on which the model was trained.

DINCAE	U-N	et32	U-N	et64
	$256 \times 256 \mid 128 \times 128 \mid$		256×256	128×128
0.54	0.45	0.43	0.44	0.42

Table 8: Comparison between our 4days-models and DINCAE.

6. Ablation and additional experiments

Many of our ablation studies have already been discussed in Section 4. In this section, we briefly report on additional experiments related to different methodological choices, neural models, and network configurations.

From a methodological perspective, before adopting the current approach — computing the residual temperature relative to seasonality — we attempted to directly reconstruct the SST. While the results were acceptable, they consistently showed a performance decrease of around 10%. In this scenario, including seasonality as an input generally led to faster and more stable training as well as improved final performance.

Regarding the models, a major class we tested were diffusion models [24, 25], which we have recently applied successfully to downscaling [28] and precipitation nowcasting tasks [29]. Despite our efforts, we were unable to achieve competitive performance with diffusion models in this case.

We tested numerous additional variants of U-Net and ViT, tuning their architectures and incorporating more sophisticated layers. Specifically, we experimented with inception modules [30], Bottleneck Attention Modules

(BAM) [31], Convolutional Block Attention Modules (CBAM) [32], and Attention-Aware layers [18]. However, none of these mechanisms led to significant performance improvements.

7. Conclusions

This study investigated deep neural networks to fill Sea Surface Temperture (SST) data gaps caused by cloud occlusion, focusing on improving data completeness and reliability.

Our findings indicate that deep learning approaches, if properly tuned on spatial and temporal dimensions, significantly improve SST reconstruction accuracy.

Comparisons with existing methods, including L4 reconstructions and other data-driven models, highlight the effectiveness of deep learning in achieving reliable SST reconstructions. Notably, our selected architectures capture finer details in SST variations, suggesting their potential to improve upon conventional reanalysis techniques that are often limited by spatial smoothing, and allowing for a more robust understanding of SST variability.

In the future, we plan to extend the analysis to the full Mediterranean area, and to incorporate data with microwave measurements, both for training and validation purposes. This could further enhance reconstruction accuracy, allowing models to adapt to various environmental conditions and providing a more comprehensive view of SST dynamics.

In summary, our results underscore the potential of deep learning to enhance SST data completeness and accuracy, offering promising applications in climate science, marine research, and oceanographic studies. This approach represents a significant step forward in SST reconstruction, enabling a deeper understanding of the complex processes that drive our climate system.

Code and Data

The code developed in this work is available in the GitHub repository at the following url: https://github.com/asperti/SST_reconstruction. Main datasets may be accessed trough the notebooks in the repository or downloaded from the sites specified in the work.

Acknowledgements

This research was partially funded and supported by the following Projects:

- Future AI Research (FAIR) project of the National Recovery and Resilience Plan (NRRP), Mission 4 Component 2 Investment 1.3 funded from the European Union NextGenerationEU.
- ISCRA Project "AI for weather analysis and forecast" (AIWAF2)

References

- [1] D. Wylie, D. L. Jackson, W. P. Menzel, J. J. Bates, Trends in global cloud cover in two decades of HIRS observations, Journal of climate 18 (15) (2005) 3021–3031.
- [2] F. P. Bretherton, R. E. Davis, C. Fandry, A technique for objective analysis and design of oceanographic experiments applied to mode-73 23 (7) (1976) 559–582.
- [3] A. Alvera-Azcárate, A. Barth, D. Sirjacobs, F. Lenartz, J.-M. Beckers, Data interpolating empirical orthogonal functions (dineof): a tool for geophysical data analyses, Mediterranean Marine Science (2011) 5–11.
- [4] S. Jung, C. Yoo, J. Im, High-resolution seamless daily sea surface temperature based on satellite data fusion and machine learning over kuroshio extension, Remote. Sens. 14 (3) (2022) 575. doi:10.3390/ RS14030575.
 - URL https://doi.org/10.3390/rs14030575
- [5] L. Ćatipović, F. Matić, H. Kalinić, Reconstruction methods in oceano-graphic satellite data observation—a survey, Journal of Marine Science and Engineering 11 (2) (2023). doi:10.3390/jmse11020340. URL https://www.mdpi.com/2077-1312/11/2/340
- [6] B. Buongiorno Nardelli, C. Tronconi, A. Pisano, R. Santoleri, High and ultra-high resolution processing of satellite sea surface temperature data over southern european seas in the framework of myocean project, Remote Sensing of Environment 129 (2013) 1-16. doi:https://doi.org/10.1016/j.rse.2012.10.012. URL https://www.sciencedirect.com/science/article/pii/ S003442571200394X

- [7] T. M. Chin, J. Vazquez-Cuervo, E. M. Armstrong, A multi-scale high-resolution analysis of global sea surface temperature, Remote sensing of environment 200 (2017) 154–169.
- [8] R. Fablet, P. H. Viet, R. Lguensat, Data-driven models for the spatiotemporal interpolation of satellite-derived sst fields, IEEE Transactions on Computational Imaging 3 (4) (2017) 647–657.
- [9] A. Barth, A. Alvera-Azcárate, M. Licer, J.-M. Beckers, Dincae 1.0: a convolutional neural network with error estimates to reconstruct sea surface temperature satellite observations, Geoscientific Model Development 13 (3) (2020) 1609–1622.
- [10] A. Barth, A. Alvera-Azcárate, C. Troupin, J.-M. Beckers, Dincae 2.0: multivariate convolutional neural network with error estimates to reconstruct sea surface temperature satellite and altimetry observations, Geoscientific Model Development 15 (5) (2022) 2183–2196.
- [11] Z. Han, Y. He, G. Liu, W. Perrie, Application of dincae to reconstruct the gaps in chlorophyll-a satellite observations in the south china sea and west philippine sea, Remote Sensing 12 (3) (2020) 480.
- [12] E. Goh, A. R. Yepremyan, J. Wang, B. Wilson, Maesstro: Masked autoencoders for sea surface temperature reconstruction under occlusion, EGUsphere 2023 (2023) 1–20.
- [13] S. Iizuka, E. Simo-Serra, H. Ishikawa, Globally and locally consistent image completion, ACM Trans. Graph. 36 (4) (2017) 107:1-107:14. doi: 10.1145/3072959.3073659.
 URL https://doi.org/10.1145/3072959.3073659
- [14] G. Liu, F. A. Reda, K. J. Shih, T. Wang, A. Tao, B. Catanzaro, Image inpainting for irregular holes using partial convolutions, in: Computer Vision ECCV 2018 15th European Conference, Munich, Germany, September 8-14, 2018, Proceedings, Part XI, 2018, pp. 89–105. doi: 10.1007/978-3-030-01252-6_6. URL https://doi.org/10.1007/978-3-030-01252-6_6
- [15] H. Liu, B. Jiang, Y. Song, W. Huang, C. Yang, Rethinking image inpainting via a mutual encoder-decoder with feature equalizations, in:

- Computer Vision ECCV 2020 16th European Conference, Glasgow, UK, August 23-28, 2020, Proceedings, Part II, 2020, pp. 725-741. doi:10.1007/978-3-030-58536-5_43. URL https://doi.org/10.1007/978-3-030-58536-5_43
- [16] J. Peng, D. Liu, S. Xu, H. Li, Generating diverse structure for image inpainting with hierarchical VQ-VAE, in: IEEE Conference on Computer Vision and Pattern Recognition, CVPR 2021, virtual, June 19-25, 2021, 2021, pp. 10775-10784. doi:10.1109/CVPR46437.2021.01063. URL https://openaccess.thecvf.com/content/CVPR2021/html/Peng_Generating_Diverse_Structure_for_Image_Inpainting_With_Hierarchical_VQ-VAE_CVPR_2021_paper.html
- [17] Z. Wan, J. Zhang, D. Chen, J. Liao, High-fidelity pluralistic image completion with transformers, in: 2021 IEEE/CVF International Conference on Computer Vision, ICCV 2021, Montreal, QC, Canada, October 10-17, 2021, 2021, pp. 4672–4681. doi:10.1109/ICCV48922.2021.00465. URL https://doi.org/10.1109/ICCV48922.2021.00465
- [18] C. Zheng, T. Cham, J. Cai, D. Q. Phung, Bridging global context interactions for high-fidelity image completion, in: IEEE/CVF Conference on Computer Vision and Pattern Recognition, CVPR 2022, New Orleans, LA, USA, June 18-24, 2022, 2022, pp. 11502-11512. doi:10.1109/CVPR52688.2022.01122. URL https://doi.org/10.1109/CVPR52688.2022.01122
- [19] J. Jain, Y. Zhou, N. Yu, H. Shi, Keys to better image inpainting: Structure and texture go hand in hand, in: IEEE/CVF Winter Conference on Applications of Computer Vision, WACV 2023, Waikoloa, HI, USA, January 2-7, 2023, 2023, pp. 208-217. doi:10.1109/WACV56688.2023.00029.
 URL https://doi.org/10.1109/WACV56688.2023.00029
- [20] P. J. Werdell, B. A. Franz, S. W. Bailey, G. C. Feldman, E. Boss, V. E. Brando, M. Dowell, T. Hirata, S. J. Lavender, Z. Lee, et al., Generalized ocean color inversion model for retrieving marine inherent optical properties, Applied optics 52 (10) (2013) 2019–2037.
- [21] N. Pinardi, M. Zavatarelli, M. Adani, G. Coppini, C. Fratianni, P. Oddo, S. Simoncelli, M. Tonani, V. Lyubartsev, S. Dobricic, et al., Mediter-

- ranean sea large-scale low-frequency ocean variability and water mass formation rates from 1987 to 2007: A retrospective analysis, Progress in Oceanography 132 (2015) 318–332.
- [22] O. Ronneberger, P. Fischer, T. Brox, U-net: Convolutional networks for biomedical image segmentation, in: Medical Image Computing and Computer-Assisted Intervention - MICCAI 2015 - 18th International Conference Munich, Germany, October 5 - 9, 2015, Proceedings, Part III, 2015, pp. 234–241.
- [23] A. Dosovitskiy, L. Beyer, A. Kolesnikov, D. Weissenborn, X. Zhai, T. Unterthiner, M. Dehghani, M. Minderer, G. Heigold, S. Gelly, J. Uszkoreit, N. Houlsby, An image is worth 16x16 words: Transformers for image recognition at scale, in: 9th International Conference on Learning Representations, ICLR 2021, Virtual Event, Austria, May 3-7, 2021, 2021.
 URL https://openreview.net/forum?id=YicbFdNTTy
- [24] J. Ho, A. Jain, P. Abbeel, Denoising diffusion probabilistic models, in: H. Larochelle, M. Ranzato, R. Hadsell, M. Balcan, H. Lin (Eds.), Advances in Neural Information Processing Systems 33: Annual Conference on Neural Information Processing Systems 2020, NeurIPS 2020, December 6-12, 2020, virtual, 2020.
 URL https://proceedings.neurips.cc/paper/2020/hash/
- [25] J. Song, C. Meng, S. Ermon, Denoising diffusion implicit models, in: 9th International Conference on Learning Representations, ICLR 2021, Virtual Event, Austria, May 3-7, 2021, OpenReview.net, 2021. URL https://openreview.net/forum?id=St1giarCHLP

4c5bcfec8584af0d967f1ab10179ca4b-Abstract.html

[26] A. Vaswani, N. Shazeer, N. Parmar, J. Uszkoreit, L. Jones, A. N. Gomez, L. Kaiser, I. Polosukhin, Attention is all you need, in: Advances in Neural Information Processing Systems 30: Annual Conference on Neural Information Processing Systems 2017, December 4-9, 2017, Long Beach, CA, USA, 2017, pp. 5998–6008.
URL https://proceedings.neurips.cc/paper/2017/hash/3f5ee243547dee91fbd053c1c4a845aa-Abstract.html

- [27] A. Vaswani, N. Shazeer, N. Parmar, J. Uszkoreit, L. Jones, A. N. Gomez, L. u. Kaiser, I. Polosukhin, Attention is all you need, in: I. Guyon, U. V. Luxburg, S. Bengio, H. Wallach, R. Fergus, S. Vishwanathan, R. Garnett (Eds.), Advances in Neural Information Processing Systems, Vol. 30, Curran Associates, Inc., 2017.
 URL https://proceedings.neurips.cc/paper_files/paper/2017/file/3f5ee243547dee91fbd053c1c4a845aa-Paper.pdf
- [28] F. Merizzi, A. Asperti, S. Colamonaco, Wind speed super-resolution and validation: from ERA5 to CERRA via diffusion models, Neural Computing and Applications (2024). URL https://doi.org/10.1007/s00521-024-10139-9
- [29] A. Asperti, F. Merizzi, A. Paparella, G. Pedrazzi, M. Angelinelli, S. Colamonaco, Precipitation nowcasting with generative diffusion models, Applied Intelligence To appear (2024).
- [30] C. Szegedy, W. Liu, Y. Jia, P. Sermanet, S. E. Reed, D. Anguelov, D. Erhan, V. Vanhoucke, A. Rabinovich, Going deeper with convolutions, in: IEEE Conference on Computer Vision and Pattern Recognition, CVPR 2015, Boston, MA, USA, June 7-12, 2015, 2015, pp. 1-9. doi:10.1109/CVPR.2015.7298594.
 URL https://doi.org/10.1109/CVPR.2015.7298594
- [31] J. Park, S. Woo, J. Lee, I. S. Kweon, BAM: bottleneck attention module, in: British Machine Vision Conference 2018, BMVC 2018, Newcastle, UK, September 3-6, 2018, 2018, p. 147. URL http://bmvc2018.org/contents/papers/0092.pdf
- [32] S. Woo, J. Park, J. Lee, I. S. Kweon, CBAM: convolutional block attention module, in: Computer Vision ECCV 2018 15th European Conference, Munich, Germany, September 8-14, 2018, Proceedings, Part VII, 2018, pp. 3–19. doi:10.1007/978-3-030-01234-2_1. URL https://doi.org/10.1007/978-3-030-01234-2_1